3D printed electronic materials and devices

13

Ruitao Su, Sung Hyun Park, Zhaohan Li, Michael C. McAlpine
Department of Mechanical Engineering, University of Minnesota, Minneapolis, MN, United States

13.1 Introduction

Significant advances have been made in advancing wearable flexible and stretchable electronics by combining thin microfabricated metallic and semiconducting components with soft substrates and encapsulations [1,2]. These methods have the advantage of creating a high yield of devices with reproducible and stable performances by taking advantage of well-established semiconductor technologies and processes. An alternative strategy is the direct printing of materials and devices without requiring cleanroom facilities. Inkjet printing has been used to print various electronic devices [3,4]. However, the ink selection for inkjet printing is limited to fluids with relatively low viscosities (the typical viscosity is limited to ca. $2–10^2$ mPa s), and therefore the technique has difficulty when creating thick, 3D structured features [5,6]. Extrusion-based 3D printing, also called direct ink writing, is capable of printing active structures and devices onto both planar and curvilinear surfaces. Because the inks are dispensed pneumatically, viscosities of inks could span a much wider range (up to 10^6 mPa s) and with disparate properties, including solutions, colloids, liquid metals, polymeric resins, etc. [7,8]. The methodology of 3D printing active electronics with both conducting and semiconducting materials has recently been patented [9].

Section 13.2 of the chapter introduces a 3D printing platform that was developed by our group to fully 3D print functional electronic devices without being tethered to a microfabrication facility. Specifics of the 3D printer and available inks for the printing platform, as well as various devices that have been printed, are overviewed. Further, the prospects of autonomous 3D printing are discussed by introducing a delta robot-based printer that is under development, as well as two commercial printers that are compact and portable. Section 13.3 discusses two types of 3D printed light emitting diodes (LEDs), consisting of CdSe-ZnS quantum dots (QDs) or silicon nanocrystals (SiNCs) as the emissive layers. The properties of these inks, including work function, band structure, quantum effects, and curing conditions are discussed. At the device level, performances of fully 3D printed LEDs and more complex structures with embedded LEDs are discussed. Further, a fundamental challenge in the printing of high-quality electronics with uniform performance—achieving homogeneity in the printed layers—is analyzed with a capillary flow model during the evaporation of the deposited ink droplet. To improve the homogeneity of the printed patterns,

Robotic Systems and Autonomous Platforms. https://doi.org/10.1016/B978-0-08-102260-3.00013-5

concentration gradient–induced Rayleigh flow and surface tension–induced Marangoni flow are proposed to balance the migration of solutes during evaporation. Finally, a flexible tactile sensor and inductive coil printed on the body are introduced in Section 13.4. Room temperature curable inks that are highly conductive and stretchable are critical factors to obtaining electronics printed directly on the body. The printed tactile sensors exhibit high stretchability and sensitivity, while the adaptively printed inductive coil demonstrates wireless powering. In addition, interfacial mechanics of epidermal electronics are investigated in order to propose methodologies for creating conformal and intimate interfaces between 3D printed electronics and human skin.

13.2 3D printing systems

Based on the methodology of how structures are deposited and solidified, 3D printing can be categorized into two broad classes: light-based and ink-based printing [8]. Generally, light-based printing employs focused laser beams to solidify polymeric inks in a layer-by-layer manner via a prescribed geometrical model. Photoinitiators are typically added to accelerate the cross-linking of polymeric molecules upon illumination by the laser beams. On the other hand, depending on the mechanism of ink deposition, ink-based 3D printing can be classified as inkjet printing or extrusion-based 3D printing. Inkjet printing dispenses inks, activated via thermal or acoustic mechanisms, at high frequencies in the form of liquid droplets onto substrates [6]. In the case of ink-extrusion-based 3D printing, inks such as melted plastic filaments, viscous polymers, or liquid droplets are extruded from printing nozzles, activated pneumatically (often with solenoid valves to control air flow). Due to the high-precision computer numerical control (CNC) system that is available from industrial robots, 3D printers adapted from these robotic systems can in principle execute motions with resolutions down to tens of nanometers.

13.2.1 Ink extrusion–based 3D printing platform

The custom-built 3D printing platforms that are discussed in this chapter have demonstrated the ability to print functional devices including electronics [7,10], soft robotics [11], organ models [12], and biological materials [13]. Although varying in design, the 3D printing platforms typically consist of the following key subsystems: a computer numerically controlled (CNC) navigated translational module (including vertical and horizontal modules), a real-time imaging system, a pneumatically controlled ink-dispensing system, and a UV generating system for the curing of printed structures (Fig. 13.1A). For instance, the Aerotech AGS1000 Cartesian gantry system has a motion resolution of 10 nm vertically and 1 μm horizontally, thus providing a high-precision platform for printing mesoscale constructs. Devices from the micro- to the macroscale can be printed within a workspace of 300 mm (X) × 400 mm (Y) × 100 mm (Z), achieving multiscale manufacturing. For instance, 3D printed LEDs can achieve an overall size of ∼2 mm, while the width of the printed conductive

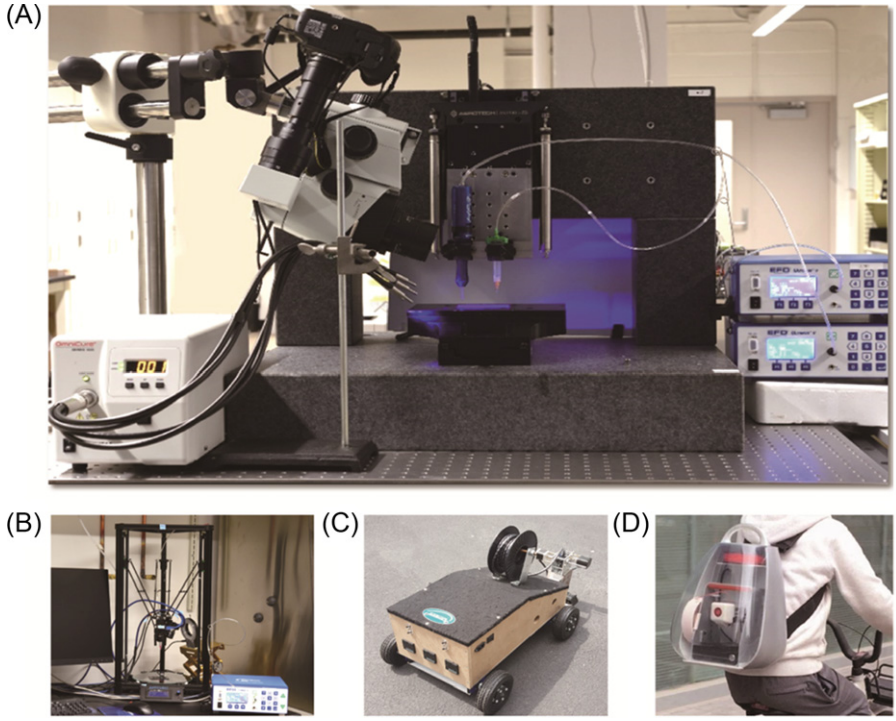

Fig. 13.1 Custom-built and commercial 3D printers. (A) Custom-built ink extrusion-based 3D printing platform consisting of a motion module, real-time imaging module, pressure control module and a UV-light generating module. (B) Custom-built 3D printer based on a delta robot that can adaptively print on moving objects with closed-loop control [14]. (C) Vehicular 3D printer by Addibots that can print industry-standard materials onto the ground while driving autonomously. (D) Compact and portable MIGO 3D printer by MakeX that can continuously print while being carried in a backpack [15]. (C) is adapted with permission from Addibots, LLC., ©2016 Addibots, LLC. (D) is adapted with permission from MakeX, ©2017 MakeX.

traces is ≦100 μm [7], whereas the lateral dimensions of 3D printed organ models are on the scale of several centimeters [12]. In addition, the brushless linear servomotors have a maximum translational speed of 2 m/s, which is beneficial to the precise patterning of repetitive features for which the uniform and fast illumination by UV light is critical. A flexible G-code compilation environment renders printing from both CAD models and self-designed trajectories. Lastly, the printing of multimaterial and multifunctional devices requires the compositional inks to be deposited precisely and sequentially onto prescribed coordinates. The two separately controlled vertical axes of the 3D printing platform can be mounted with multiple ink reservoirs; therefore, the autonomous switching of inks increases the consistency of the printed devices in terms of the alignment of adjacent layers.

In the case of 3D printed electronic devices, the broad range of available inks, e.g., conducting, semiconducting and dielectric inks, allows for flexibility in the bottom-up design of both active and passive components. To date, the demonstration of 3D printed electronic devices has covered most of the basic elements conventionally fabricated by semiconductor technologies, including storage devices such as batteries and capacitors [16], inductors [17], LEDs [7], stretchable sensors [10], and actuators [11,18]. The printing of these devices is enabled by the ability to print functional materials over multiple length scales. For instance, colloids or pastes of metallic nanoparticles can be printed as both conductive traces and active components. Silver nanoparticles (AgNPs) dispersed in organic solvents have been printed as electrodes for quantum dot LEDs [7] and interconnects in electronic circuits [19]. High conductivity (within two orders of magnitude of bulk silver) of the printed structures can be achieved following sintering at elevated temperatures (~140°C). Piezoresistive inks comprised of submicrometer silver particles mixed into silicone elastomers have also been printed as the sensing elements of tactile sensors [10]. For the printing of insulating structures, dielectric materials such as polydimethylsiloxane (PDMS) are often adopted due to their good printability and reasonable dielectric constants (~2.5). In the field of soft robotics, dielectric ionic hydrogels have also been printed as the active layers of strain sensors and actuators for sensing mechanical strain or executing deformations via an externally applied electric field, respectively [11,18].

13.2.2 Prospects for autonomous 3D printers

Autonomous and compact 3D printers, which can be controlled by intelligent image-scanning and code-generating programs, could play critical roles in the repair and maintenance of machines, robots, and even the human body in urgent situations such as equipment breakdown or injury on the battlefield. 3D printing functional materials and devices in a manner that is completely decoupled from any cleanroom or microfabrication facility is a paradigm-shifting concept, but one that requires significant advancements. Instead of building a CAD model and generating G-codes for 3D printing, autonomous 3D printing requires extracting the topological information of the target surface from the scanned data of the object. Guo et al. demonstrated the principles and steps of autonomous 3D printing via the printing of a stretchable tactile sensor on the fingertip of a hand model [10]. First, the hand model was scanned from different perspectives with a 3D scanner to acquire geometrical information in the form of cloud points. Then these cloud points were merged and assembled to generate a polygon-meshed model that represented the topology of the target surface. Based on the morphology of the fingertip in this rebuilt model, the printing path of the tactile sensor was designed. Finally, G-code for 3D printing was generated from the geometry of the sensor, and the printing process was performed [10]. By integrating these steps into one continuous process and implementing feedback control via real-time scanning and image processing, autonomous 3D printing with minimal human intervention could in principle be achieved. Recently, Zhu et al. demonstrated “adaptive” 3D printing of functional electronics directly onto the back of a moving hand via a

compact 3D printing system consisting primarily of a delta robot, a type of parallel manipulator [14] (Fig. 13.1B). Specifically, the closed-loop feedback control system enabled the visualization of the geometry and real-time motion of a moving freeform surface that was sent to the motion controller. The automatically generated toolpaths for the motion of the printer head were then executed by the ink extrusion–based 3D printer to print functional devices conformally onto the target surface. Soft and stretchable electronics, such as electronic skins, have been effective strategies for human-machine interfaces (HMIs) [20]. The next-generation ability to directly print functional electronics autonomously and adaptively onto robots or even the human body could enable further advances in bionics and HMIs.

Autonomous and compact 3D printers might also be rendered portable, which can enable further applications in space-limited and mobile environments. For example, one vehicular 3D printer developed by Addibots, LLC, a company focused on developing portable 3D printers, can print industry-standard materials as well as conductive materials and sensors onto the road, to enable applications such as eVehicle charging lanes, smart cities, and next generation telecom applications (Fig. 13.1C). Another example is the MIGO 3D printer, a compact printer developed by MakeX with a size of 35 cm (L) × 28 cm (W) × 50 cm (H). Due to its compactness and low power consumption, the printer can be powered by batteries and fits into a backpack to print continuously for 3 h while on the move [15] (Fig. 13.1D). This rapid progress in the miniaturization and portability of versatile 3D printers will undoubtedly facilitate broader applications in 3D printing multimaterial and multifunctional electronic devices as the printers continue to expand their capabilities.

The financial impact of 3D printed electronics is expected to be significant. According to Mahto et al., "Revenue from 3D-printed electronics and consumer products accounted for 13 percent of the larger additive manufacture (AM) industry, or $681 million, in 2015. The growth for this segment is expected to remain strong; AM industry analysts predict that 3D-printed electronics is likely to be the next high-growth application for product innovation, with its market size forecast to reach $1 billion by 2025." [21].

13.3 3D printed optoelectronic devices

Optoelectronic devices, such as LEDs, solar cells, and photodiodes (PDs), have been fabricated in two dimensions by a variety of methods, including roll-to-roll printing, vacuum thermal evaporation, and spin coating [22–25]. These devices exhibit high quality performance and can be implemented on flexible substrates. Yet, moving toward 3D architectures without utilizing sophisticated masks and stacking strategies remains a challenging task. 3D printing has demonstrated the ability to integrate functional materials, including liquid metals, particulate colloids, polymeric solutions and resins, into light emitting diodes (LEDs) with varying emission spectra, including direct bandgap quantum dot-based LEDs (QD-LEDs) [7] and even silicon nanocrystal-based LEDs (SiNC-LEDs).

13.3.1 Inks for 3D printed LEDs

13.3.1.1 Inks for electrodes and transport layers

Fig. 13.2 sketches the work functions and band structures of the materials utilized for fully 3D printed LEDs. Conventionally, indium tin oxide (ITO) is the most commonly used electrode material due to its high conductivity ($\sim 10^6$ S/m), optical transparency (>90%) and compatibility with physical or chemical vapor deposition techniques (PVD/CVD) [26,27]. One reported sol-gel process that has been utilized to spin-coat uniform, transparent, and highly conductive ITO films has demonstrated the possibility of applying this method to 3D printing [28]. However, the major challenge for 3D printing ITO lies in controlling the thickness and uniformity of the printed film, which is critical to the transparency and interface quality of the ITO electrodes [28].

Alternatively, for 3D printed optoelectronic devices, ITO film can be replaced by the composite structure of ring-shaped silver nanoparticles (AgNPs) and a poly(3,4-ethylenedioxythiophene):polystyrene sulfonate (PEDOT:PSS) film [7]. Highly conductive ($\sim 10^7$ S/m) traces printed with AgNPs connect the PEDOT:PSS layer with an external power source. It has been demonstrated that the work function of oxidized AgNPs shifts ~0.7 eV away from the vacuum following air annealing due to oxidation of the AgNPs [29,30] (Fig. 13.2). This shift is favorable for the 3D printed LEDs, since the enhanced alignment between the work function of AgNPs and PEDOT:PSS reduces the carrier transport barrier.

Conjugated polymers were discovered to be capable of constructing stable electronic architectures at the device level in the early 1990s [31]. The semiconducting properties of conjugated polymers, such as PEDOT:PSS and poly[*N*,*N*′-bis(4-butylphenyl)-*N*,*N*′-bis(phenyl)-benzidine] (poly-TPD), are attributable to the alternating single and double bonds that facilitate the delocalized π-bonding [32]. Often

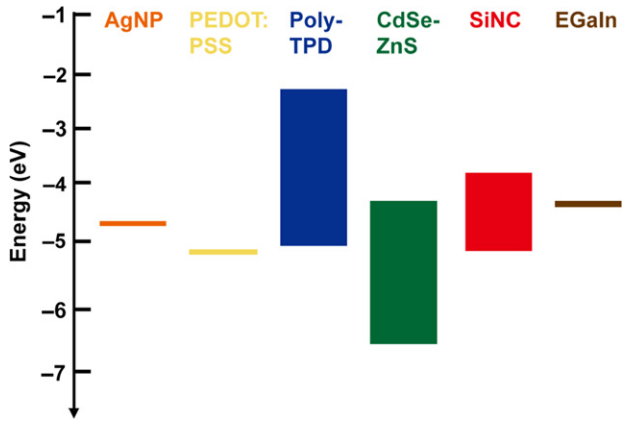

Fig. 13.2 Work functions and band structures of materials printed for LEDs. AgNPs and PEDOT:PSS were printed as the anode; poly-TPD was printed as the hole transport layer; CdSe-ZnS and SiNCs were printed as the emissive layers of QD-LEDs and SiNC-LEDs, respectively; EGaIn was printed as the top cathode of the LEDs.

employed as the transport and emissive layers of optoelectronic devices, conjugated polymers are usually processed by thermal vacuum evaporation and spin-coating [33,34]. Due to their intrinsic compatibility with solution processing, conjugated polymers have recently been utilized for 3D printed LEDs [7]. A polymer with a high conductivity of 4.6×10^5 S/m and a work function of −5.2 eV [35] (Fig. 13.2), PEDOT:PSS is often patterned as a transparent electrode or hole transport layer (HTL) for LEDs, PDs, and solar cells [36–38]. Specifically, for 3D printed LEDs, PEDOT:PSS-based inks were dispensed in the form of aqueous colloids on top of printed silver rings [7]. In this structure, because of the higher surface energy of the metals, the aqueous ink has a stronger adhesion to the metal surface (AgNPs), than the glass or plastic substrate, thus confining the printed ink droplet within the metallic electrodes [7]. This confinement defines the boundary for each individual device, electrically isolated from one another in the integrated circuit. In addition, the printed pattern can be cured in air at ∼120°C without obvious degradation in electrical properties due to the high chemical stability of the PEDOT:PSS.

For the hole transport layer, the large bandgap of poly-TPD (2.8 eV, Fig. 13.2) improves the efficiency of the device by blocking the transport of electrons toward anodes, thereby confining the exciton recombination within the emissive layer [39]. Dissolvable in most nonpolar organic solvents, inks based on poly-TPD exhibit low viscosities and therefore are dispensed by the application of pressure pulses to control the deposited volumes. It is noteworthy that the optimized concentration of inks based on poly-TPD is 10–18 × diluted compared to inks used for spin-coating due to the low material waste during fabrication [7]. Further, the fact that poly-TPD is cross-linkable by either illumination of UV light or thermal annealing in inert gas makes it resistant to organic solvents once cured, which prevents dissolution of the printed patterns after the deposition of subsequent solutions and maintains the integrity of the structure [39].

Since the hole transport layer and active layer tend to degrade at elevated temperatures, the selection of top electrodes requires inks that can be deposited at room temperature and still possess relatively high conductivities. Therefore, with a melting point of 15.5°C, eutectic gallium indium (EGaIn) was selected as the top electrode for the 3D printed LEDs. With a work function of −4.3 eV (Fig. 13.2), the good alignment of the work function of EGaIn with the electron affinity of CdSe-ZnS QDs (−4.5 eV) enabled a minimal barrier to the injection of electrons [7,40]. Further, the high surface tension (∼0.6 N/m) of the liquid metal enabled the formation of the spherical cathode once extruded from the nozzle [41]. The conductive oxide shell that forms on the surface of EGaIn once exposed to air facilitated a stronger adhesion to the substrate, which enhanced the stability of the freestanding top electrodes [42,43].

13.3.1.2 Nanoscale inks for emissive layers

Nanocrystals (NCs) smaller than the Bohr exciton radius, such as the CdSe-ZnS QDs and SiNCs that are 3D printed as the emissive layers of fully 3D printed LEDs, exhibit tunable emission wavelengths based on the sizes of the particles [40,44–46]. Narrow

emission spectra can be achieved via the synthesis of highly monodisperse particles [47]. The relationship between the size of the semiconductor particles and the energy of released photons is given by the solution to the Schrödinger equation via the "particle in a one-dimensional box" formalism, in which the confinement energy is inversely proportion to the square of the particle radius [48]. For example, LEDs printed with CdSe-ZnS core-shell QDs as the emissive layer demonstrated emission wavelengths of 550 and 615 nm by varying the sizes of the QDs [7].

Interestingly, some materials that exhibit indirect bandgaps in the bulk can emit light at small scales via a relaxation of the rule of momentum conservation, which increases the probability of a quasidirect recombination. One example is SiNC. Bulk silicon has an extremely low quantum efficiency when used as an emissive material because of the indirect bandgap of silicon, where the radiative recombination of electrons and holes is suppressed. However, this constraint can be relaxed based on the Heisenberg uncertainty principle, which states that if the size of the silicon crystal is reduced, the uncertainty in momentum broadens in k-space. Therefore, the extent of broadening is inversely proportional to the size of the SiNC [49]. This relaxation of the momentum conservation condition makes it possible for SiNCs smaller than the Bohr exciton radius (~5 nm for silicon) to display outstanding electroluminescence (EL). Indeed, SiNC-based LEDs fabricated via spin coating have achieved a remarkably high external quantum efficiency of 8.6% [39].

13.3.2 Improving the homogeneity of 3D printed patterns

Inks of nanoparticles are prepared by suspending polymer-functionalized particles in organic solvents. Parameters including concentrations of the nanoparticles, dispensing pressure, and time duration are regulated to control the volumes of deposited inks and therefore the resulting thicknesses of the printed patterns. One of the major challenges facing the electronic devices fabricated by solution-based processes, including both inkjet printing and extrusion-based 3D printing, is the uniformity of the printed patterns that determines the interfacial contact between two adjacent components. More uniform surfaces and hence more intimate contacts indicate smaller barriers to charge carrier transport and thus better performance of the devices. Although 94%–97% of the material can be conserved by 3D printing [50], the trade-off relative to spin-coating is a decrease in the homogeneity of the printed patterns due to an enlarged internal convection within the liquid droplets.

13.3.2.1 Capillary flow within a drying droplet

The well-known "coffee ring" effect, which is attributed to capillary flow during the evaporation of solvents in a liquid droplet, is the primary cause of the nonuniformity of printed patterns [51]. For organic solvent-based inks, in most cases, the droplet has a contact angle of <90 degrees: that is, one droplet wets the substrate, for which the contact line is pinned during evaporation [52]. Suppose the contact angle stays constant and there is no internal flow; then, liquid at the contact line will evaporate and the size of the droplet will shrink [51] (Fig. 13.3A). This observation leads to the

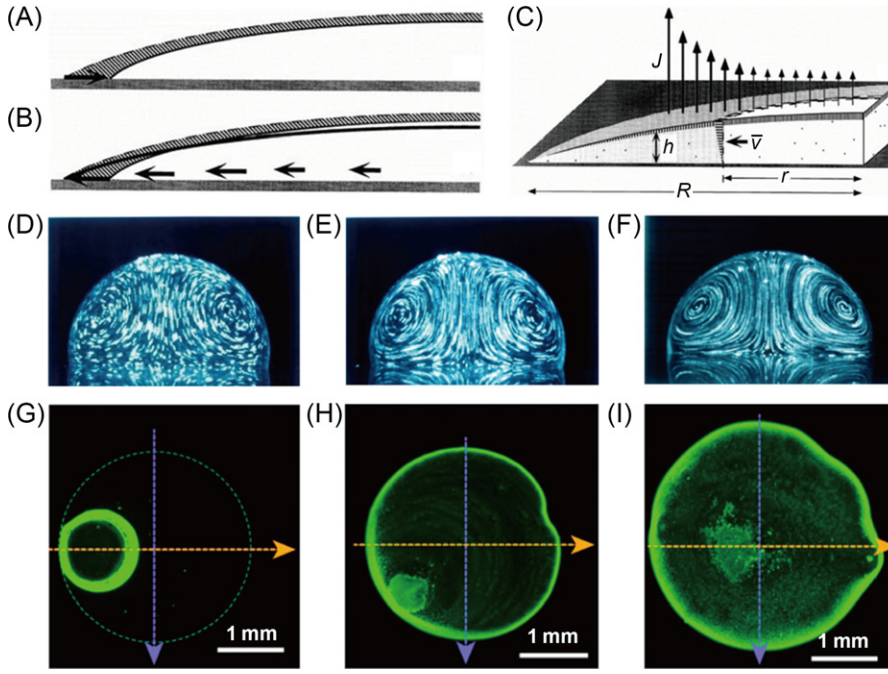

Fig. 13.3 Fluid mechanics of evaporating droplets. (A–C) Sketches of capillary flow during the evaporation of a droplet deposited onto the substrate: (A) receding contact line in the absence of internal flow; (B) capillary flow generated within the droplet with a pinned contact line; (C) sketch of the relationship between quantities that are involved in the formation of the internal capillary flow [51]. (D–F) Optical images of saline Rayleigh flow in evaporating droplets with different NaCl concentrations. The flow direction is upward for all cases: (D) 0.01 wt%, evaporation time ~39 min; (E) 0.1 wt%, evaporation time ~45.7 min; (F) 1 wt %, evaporation time ~63 min [53]. (G–I) Binary solvent mixtures that alter the deposition uniformity of CdSe-ZnS QDs: (G) 0% volume fraction of dichlorobenzene in toluene; (H) 20% volume fraction of dichlorobenzene in toluene; (I) 50% volume fraction of dichlorobenzene in toluene [7].

conclusion that there must be a radial flow toward the perimeter within the droplet to replenish the solvent loss due to the evaporation at the edge; otherwise, the contact line will recede [52] (Fig. 13.3B).

One mathematical model proposed by Deegan et al. explicitly analyzes the mass transport within the droplet. A profile of velocity and evaporation flux is sketched in Fig. 13.3C. At steady state, the diffusion equation is

$$\nabla^2 \varnothing = 0 \tag{13.1}$$

where $\varnothing(r)$ is the profile of vapor concentration around the droplet. The evaporation flux $J(r)$ can be represented as

$$J(r) = -D\nabla\varnothing \tag{13.2}$$

where D is the diffusivity of the solvent vapor in air. By solving a similar electrostatic problem where the droplet is regarded as a conductor and $\varnothing(r)$ is equivalent to the electrostatic potential [54], $J(r)$ has a diverging trend as r approaches the contact line [55]:

$$J(r) \propto (R - r)^{-\lambda} \tag{13.3}$$

where $\lambda = (\pi - 2\theta_c)/(2\pi - 2\theta_c)$ and θ_c is the contact angle of the droplet with the substrate. This expression indicates a constant profile of evaporation flux that is independent of time before the droplet dries up. In the final stage of the drying, i.e., as time approaches the dry-up time t_f ($t \to t_f$), the layer height approaches zero ($h(r) \to 0$). However, $h(r)\overline{v}(r)$ must stay constant to maintain the constant evaporation flux $J(r)$ ($h(r)\overline{v}(r) = \text{const.}$). Therefore,

$$\overline{v}(r) \propto \left(t_f - t\right)^{-1} \tag{13.4}$$

which means that the lateral transporting velocity across the droplet diverges as the drop dries up. Based on this model, as the solvent is completely evaporated, all of the solute will be deposited on the perimeter as a ring.

This simplified model neglects several important thermodynamic effects that may be present in real engineering scenarios: (i) an irregular contour at the perimeter can cause a nonuniform deposition, with the highly convex part exhibiting more solute deposition due to the higher evaporation flux [51]; (ii) a solution with a high initial concentration or large particle size will have a wider deposited ring [51]; and (iii) other thermal and fluidic effects may alter the pattern of the capillary flow and influence the final pattern of particle deposition, such as Rayleigh flow induced by the temperature/concentration gradient and Marangoni flow induced by the surface tension gradient across the surface of the solution droplet.

13.3.2.2 Mechanisms counteracting capillary flow

Based on the preceding analysis, one of the strategies to reduce the coffee ring effect is to increase the viscosities of inks and hinder the lateral transportation of solutes. For instance, during the fabrication of biosensors for lateral flow immunoassays (LFA), to overcome the coffee rings of aqueous solutions deposited by inkjet printing, Zhan et al. reported an improved uniformity of 3D printed gold nanoparticles (GNPs) by suspending the particles in glycerol with a concentration of 65 wt% [56].

More importantly, from the perspective of fluid mechanics, two recognized mechanisms can be applied to balance the outward capillary flow during the drying of a droplet deposited on a flat substrate: Rayleigh and Marangoni flow [52,53]. Rayleigh convection is the circulation induced by the buoyancy force due to the density gradient within the fluid under a gravitational field. During evaporation, the density gradient within a droplet is induced by the concentration gradient of the solutes, with the concentration close to the surface being higher [53]. As shown in Fig. 13.3D–F, the time-lapse images show that, within droplets of NaCl solutions, the intensity of internal Rayleigh convection increases with the initial concentration of NaCl. This relationship can be characterized by the dimensionless salinity Rayleigh number (R_{aS}),

$$R_{aS} = \frac{g\beta c_0 a_0^3}{\nu D} \tag{13.5}$$

where $g = 9.81$ m/s^2 is the gravitational acceleration, $\beta \equiv \frac{1}{\rho} \times \frac{\partial \rho}{\partial c}$ is the concentration expansion coefficient, c_0 is the initial concentration of solute, a_0 is the initial radius of the droplet, ν is the kinematic viscosity of the fluid, and D is molecular diffusivity of the solute. Under normal conditions (room temperature, atmosphere pressure) and with an initial concentration of 1 wt%, R_{aS} is on the order of 10^4 [53]. By controlling the magnitude of R_{aS}, one can control the intensity of the Rayleigh convection. Noticing that the direction of Rayleigh flow is upwards in the center of the droplet and inwards at the bottom, tuning the concentrations of inks during 3D printing is promising for counteracting the outward capillary flow.

Marangoni flow occurs when mass transfer is driven by a surface tension gradient that is induced by the variation of evaporation flux across the surface of the droplet. Even though a quantitative model is still to be developed for Marangoni convection in a drying droplet, it has been proven effective to use a binary solvent system that consists of two solvents with different boiling points (or different surface tensions) to achieve the uniform deposition of particle-based solutes [7,52]. For the 3D printed QD-LED, a binary solvent system consisting of toluene and dichlorobenzene was adopted to increase the uniformity of the printed QD layer by exploiting the solutal Marangoni effect. As shown in Fig. 13.3G–I, among the varying ratios of the two constitutional solvents, 20% volume fraction of dichlorobenzene in toluene generated the most ideal pattern in terms of both mass distribution and surface roughness of the deposited QD layer [7].

13.3.3 3D printed LEDs

As shown in Fig. 13.4A, the constitutional components of the QD-LED were printed in a layer-by-layer configuration. At the bottom of the device, silver nanoparticles (AgNPs) were printed as ring-shaped anodes for the purpose of light extraction. Next, an aqueous colloid of PEDOT:PSS was deposited in the center of the silver ring, which uniformly transmits the electric potential from the silver ring to the layer above it. Then, crosslinkable poly-TPD solution was printed as the hole injection layer and CdSe-ZnS core-shell QDs were printed as the emissive layer, sequentially. These two layers were both annealed in inert environments at temperatures above 100°C. Finally, EGaIn was printed as the cathode on the active layer.

As displayed in Fig. 13.4B and C, 3D printed QD-LEDs of two different colors, green and red-orange, both displayed typical electrical characteristics of diodes, with turn-on voltages of ~3 V [7]. Notably, for the 3D printed green QD-LEDs, the voltage requirement for 100 cd/cm^2 luminance was 4.5 V, whereas the voltage requirements for inkjet-printed and mist-coated QD-LEDs were 9.3 and 12.2 V, respectively [50,58]. However,

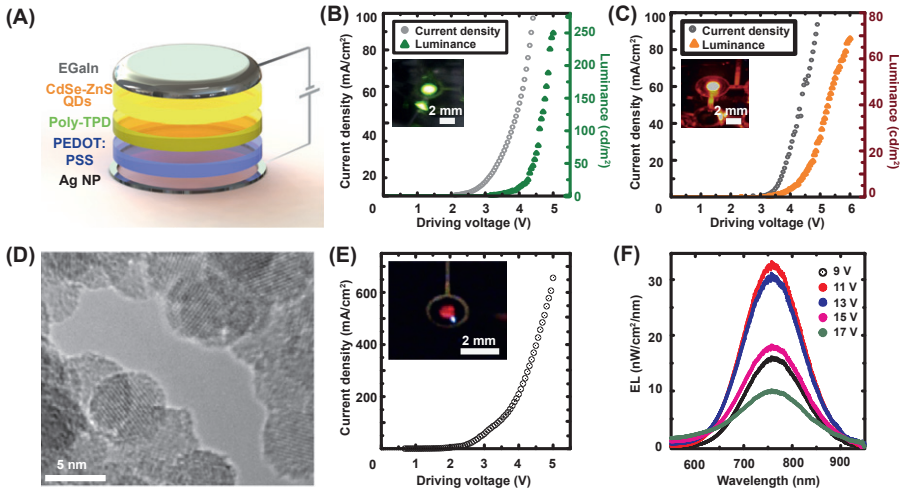

Fig. 13.4 3D printed LEDs with nanoparticles. (A) Schematic of CdSe-ZnS QD-LED. (B) *J-V-L* curves of green QD-LED. Inset: EL of QD-LED with peak wavelength ~550 nm. (C) *J-V-L* curves of orange QD-LED. Inset: EL of QD-LED with peak wavelength ~615 nm [7]. (D) Transmission electron microscopy (TEM) image of silicon nanocrystals with size ~5 nm [57]. (E) *J-V* curve of SiNC-LED. Inset: EL image of SiNC-LED with a peak wavelength ~760 nm. (F) EL spectrum of SiNC-LED under varying driving voltages.
Figures (A)–(C) are adapted with permission from Y.L. Kong, I. A. Tamargo, H. Kim, B.N. Johnson, M.K. Gupta, T.W. Koh, H.A. Chin, D.A. Steingart, B.P. Rand, M.C. McAlpine, 3D printed quantum dot light-emitting diodes, Nano Lett. 14 (2014) 7017–7023, © 2014 American Chemical Society. Figure (D) is adapted with permission from U.R. Kortshagen, R.M. Sankaran, R.N. Pereira, S.L. Girshick, J.J. Wu, E.S. Aydil, Nonthermal plasma synthesis of nanocrystals: fundamental principles, materials, and applications, Chem. Rev. 116 (2016) 11061–11127, © 2016 American Chemical Society.

LEDs fabricated with more mature methods such as transfer printing and spin coating have reported luminances of 2300 and 24,000 cd/cm^2, respectively, at 5 V [59]. Therefore, the performances of 3D printed LEDs could be dramatically improved by controlling the fluid transport mechanisms during fabrication.

Even though quantum dots such as CdSe have been applied to bioimaging and drug delivery, the cytotoxicity of CdSe is a limiting factor for wider biomedical applications due to the desorption of Cd ions [60]. In contrast, SiNCs synthesized by liquid phase reaction have been proven highly biocompatible, with applications including fluorescent probes in cellular imaging and cancer-related in vivo applications such as tumor vasculature targeting and sentinel lymph node mapping [61,62]. Therefore, 3D printed SiNC-LEDs hold promise for applications in areas such as cancer diagnosis and optogenetics.

SiNCs that were 3D printed as the emissive layer were synthesized in a nonthermal plasma reactor [57]. Fig. 13.4D shows a transmission electron microscopy (TEM) image of SiNCs in which the crystal lattice of silicon can be observed. Similar printing procedures to QD-LEDs were implemented for SiNC-LEDs. Fig. 13.4E displays the *I-V* characteristics of the 3D printed SiNC-LEDs with a turn-on voltage ~2.5 V, as well as the red-IR illumination of one SiNC-LED in the inset. In addition, as displayed in Fig. 13.4F, by confining the particle sizes in the range of 3–5 nm, 3D printed SiNC-LEDs exhibited a relatively pure light emission with a peak wavelength of 755 nm. It is noticeable that the 11 V driving voltage generated the maximum EL intensity, because higher driving voltages induce harsher thermal conditions that accelerate the oxidation of SiNCs, which indicates that better encapsulation and thermal management are demanded to enhance the performance of 3D printed LEDs.

Printing electronic devices onto freeform and curvilinear surfaces, which has potential applications in wearable displays, sensors embedded on contact lenses, and direct printing of electronics on the body, can be realized via the combination of 3D structured-light scanning (SLS) and 3D printing [63–66]. To demonstrate the capability of printing functional LEDs on curvilinear surfaces, QD-LEDs were printed onto the surface of a contact lens with intimate and conformal interfacial contact. By reconstructing the topology of the contact lens from scanned data, the corresponding printing pathways of LEDs can be designed [7]. Fig. 13.5A shows the scanned geometry of one contact lens and constitutional layers of the QD-LED that is to be printed on it. The EL of one QD-LED that was printed onto a 3D scanned contact lens is shown in Fig. 13.5B. Further, the ability to fabricate devices in a layer-by-layer manner opens the possibility of integrating active electronics with biological tissues, which could enable the creation of bionic organs with augmented functionalities [13,67]. As a demonstration of the concept of interweaving electronics into 3D structured soft constructs, a $2 \times 2 \times 2$ cube of encapsulated LEDs interconnected via horizontal and vertical conductive traces were 3D printed using silicone as the scaffold [7]. Fig. 13.5C displays a schematic of the architecture, and Fig. 13.5D shows the EL from one LED embedded in the matrix. The multidimensional and multicolor LED matrix allows for external 3D printed addresses to each embedded LED, setting the stage for future prospects in 3D printed holographic displays [7].

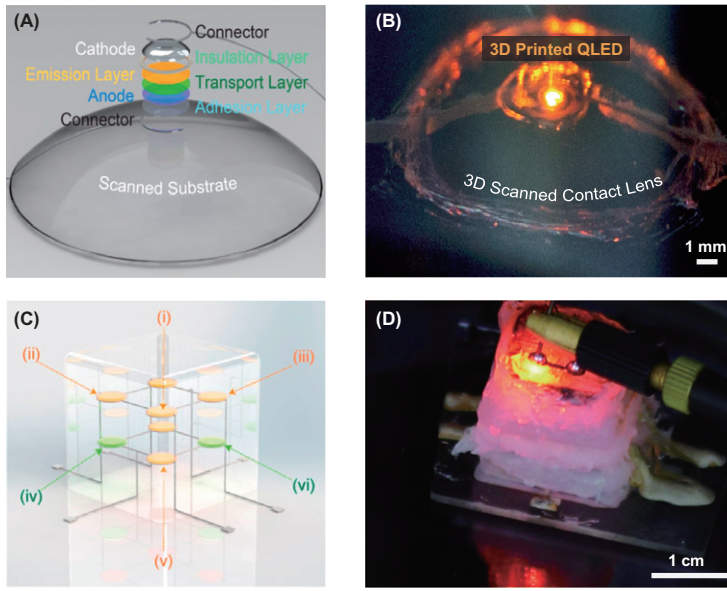

Fig. 13.5 3D printed QD-LEDs in 3D structures. (A) CAD model of 3D printed QD-LED on a 3D scanned contact lens. (B) EL of QD-LED 3D printed onto the contact lens. (C) 3D model of a multicolor, multidimensional QD-LED matrix. (D) EL of one of the QD-LEDs embedded in a silicone-based matrix [7].
Figures (A)–(D) are adapted with permission from Y.L. Kong, I. A. Tamargo, H. Kim, B.N. Johnson, M.K. Gupta, T.W. Koh, H.A. Chin, D.A. Steingart, B.P. Rand, M.C. McAlpine, 3D printed quantum dot light-emitting diodes, Nano Lett. 14 (2014) 7017–7023, © 2014 American Chemical Society.

13.4 3D printed electronics on the body

The ability to directly 3D print electronics onto the human body using multifunctional inks is an exciting prospect for expanding beyond conventional electronics, which are planar and rigid. The advantages of 3D printing in this area are threefold: (1) 3D printing allows for patterning of electronic materials over multidimensional and multiscale surfaces that are characteristic of biology and distinct from planar conventional electronics; (2) nanoscale inks can be generated that exhibit high performance and functionality but without the mechanical rigidity and brittleness of planar wafers such as Si (Young's modulus = 150 GPa), such that functional inks can be interwoven with soft 3D printed polymers and hydrogels; and 3) these functional inks can be synthesized at high temperatures to generate nanocrystalline materials with high performance, but then can subsequently be assembled under ambient conditions via the extrusion-based 3D printing process. Impact arenas such as wearable electronics [68], on-body energy harvesting [69], and bionic skins [70] are critical areas that can benefit from the intimate and compliant interface between biological tissue and electronics allowed by 3D printing. To date, tactile sensors and inductive coils that are 3D printed onto hand models and directly on human skin, respectively, have been demonstrated [10,14].

13.4.1 Room temperature curable silver-based conductive inks

Since printing electronics onto the human body needs to be performed under ambient conditions to avoid harsh curing conditions, the composition of the active inks is a critical aspect that should be tailored based on several criteria [10,14]. Tunable rheological properties are necessary to ensure a smooth flow of the inks through the nozzle, especially when printing with nozzles that have small diameters. A certain degree of flexibility that accommodates the deformation of skin during body part motion should be preserved while maintaining sufficient structural integrity and electrical connectivity of the printed structure. Electrical properties such as conductivities and piezoresistivities need to closely match bulk properties, yet be adjustable based on the composition of the ink to meet individual device and situational requirements. Finally, the ink should ideally be biocompatible and not cause adverse reactions or rashes to the skin, while being cured relatively quickly under mild conditions once printed onto the body.

For the active layer of biointegrated tactile sensors, stretchability and piezoresistivity are important for the performance of the sensor in terms of response, sensitivity, and stability. The ink for the sensing layer was developed by mixing submicrometer-sized silver particles within a highly stretchable silicone elastomer (Dragon Skin 10) that is curable at room temperature [71]. Fig. 13.6A displays an SEM image of the ink with 68 wt% of silver particles. The size range of the selected silver particles eliminates the necessity of applying high temperature to create conductive networks within the ink, which is typically necessary for nanoparticle-based inks. The stretchability of the ink decreased with increasing content of silver particles in the elastomeric silicone, although a tensile strength of ~250% is still maintained with 75 wt% of silver particles [10]. Considering a balance between conductivity and stretchability, inks with 75 wt% concentration of silver particles were chosen for the electrodes. At the percolation threshold that occurs at a content of 67.45 wt% silver particles, the ink displayed maximally sensitive piezoresistive properties. As displayed in Fig. 13.6B, for inks at this percolation threshold, a continuous increase of applied pressure to the test specimen led to a decrease in the resistance by more than two orders of magnitude [10]. Thus, these inks were selected for the sensing coil component.

For printing conducting inks directly on the body, biocompatibility and the ability to exhibit fast curing while still achieving high conductivity are critical to the functionality of the device and the validation of the concept of direct on-body printing of highly functional inks. Poly(ethylene oxide) (PEO) is a biocompatible polymer that is widely used in microbiology and medication [72,73], and here was adopted as the matrix of the composite ink, offering high viscosity and mechanical strength. Micro-sized silver flakes were added as the conductive filler, achieving a conductivity of $1.38 \pm 0.0814 \times 10^4$ S/cm at a silver concentration of 88 wt% [14]. Fig. 13.6C displays an SEM image of the composite ink following extrusion from the printing nozzle. Importantly, a mixture of water and ethanol was used as the solvent to adjust the rheological properties of the ink. The ratio of ethanol can be increased to reduce the curing time of the printed ink (Fig. 13.6D). With an ethanol content of 80 wt% in the solvent, the resistance of the printed electrode decreased by 90% within 10 min, such that the printed device became functional shortly after direct printing on the body [14].

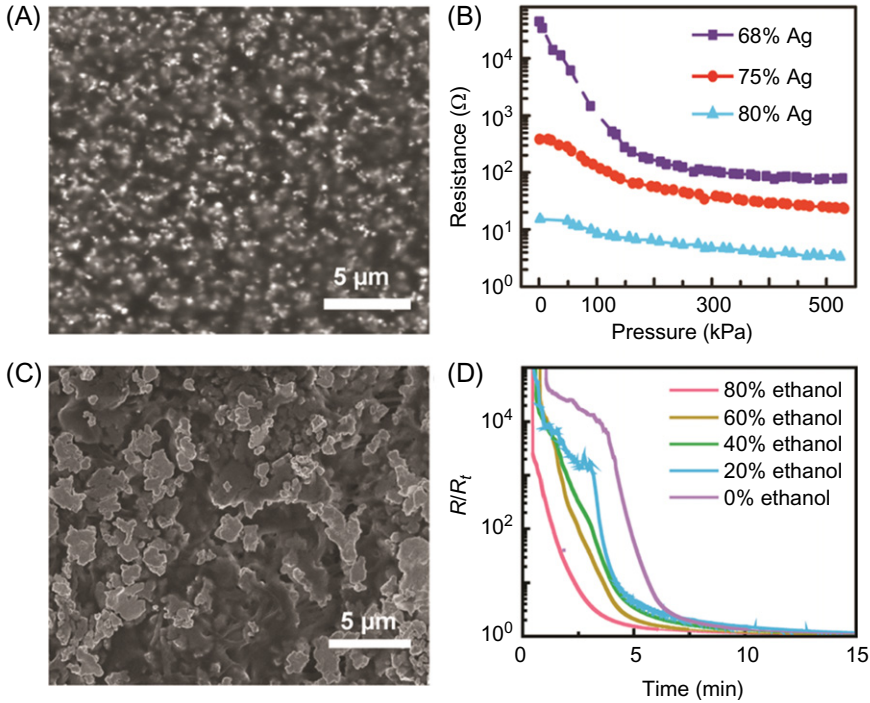

Fig. 13.6 Ag-based inks 3D printed for tactile sensors and inductive coils. (A) SEM image of well-dispersed AgNPs in silicone elastomer with 68 wt% Ag concentration used for 3D printing tactile sensors [10]. (B) Resistance-pressure characteristics of inks with varying Ag concentrations [10]. (C) SEM images showing microsized Ag flakes within extruded inks for the 3D printing of inductive coils. (D) Relative resistance as a function of time displays the fast curability of the 3D printed ink under room temperature conditions. R_t is the resistance of the printed ink following exposure to ambient for 30 min [14].
Figures (A) and (B) are adapted with permission from S.Z. Guo, K. Qiu, F. Meng, S.H. Park, M.C. McAlpine, 3D printed stretchable tactile sensors, Adv. Mater. 29 (2017) 1701218, © Wiley 2017. Figures (C) and (D) are adapted with permission from Z. Zhu, S.-Z. Guo, T. Hirdler, C. Eide, X. Fan, J. Tolar, M.C. McAlpine, 3D printed functional and biological materials on moving freeform surfaces, *Adv. Mater. 30* (2018) 1707495, © Wiley 2018.

13.4.2 3D printed sensors and wireless power on the body

Combined with the development of novel functional inks, 3D printing has potential for the extraordinary concept of printing functional electronics directly on the body via a portable printer, without requiring a microfabrication facility. In the case of the 3D printed tactile sensor, in addition to the sensing and electrode layers printed with silver-containing inks, two other component layers, a base layer and an insulating layer, were printed with the Dragon Skin 10 that was modified by a thickening agent and curing retarder [10]. With a failure strain of 1000%, Dragon Skin 10 provided the 3D printed tactile sensor with high stretchability and stable insulation between electrodes [74,75]. From the perspective of mechanical behavior, due to the silicone-based

active layer, the tactile sensor displayed typical viscoelastic behavior in which the storage (E') and loss (E'') moduli increased as the applied dynamic strain increased [10]. Further, finite element analysis (FEA) confirmed that the compressive loading to the sensor primarily occured in the sensing layer [10]. The electromechanical sensitivity of the sensor was characterized by the gauge factor (GF) [76], and the GF of the tactile sensor was of the same magnitude as single crystal silicon and other recent nanomaterial-based strain gauges [70,76–78]. Fig. 13.7A shows an SEM image of one submillimeter-sized sensing element in the sensing layer that exhibited a variation in resistance once compressed. Importantly, combined with 3D SLS, the use of 3D printing to fabricate electronics onto freeform surfaces was demonstrated by conformally printing the strain sensor onto the finger tip of a hand model [10] (Fig. 13.7B). Fig. 13.7C displays the current response of the tactile sensor when compression of various magnitudes was applied by a human finger [10]. Lastly, a 5 × 5 sensor array was 3D printed to detect spatially resolved pressure information, which opens new avenues in the promising application of 3D printing for large-scale electronic skins and wearable biomedical devices [10].

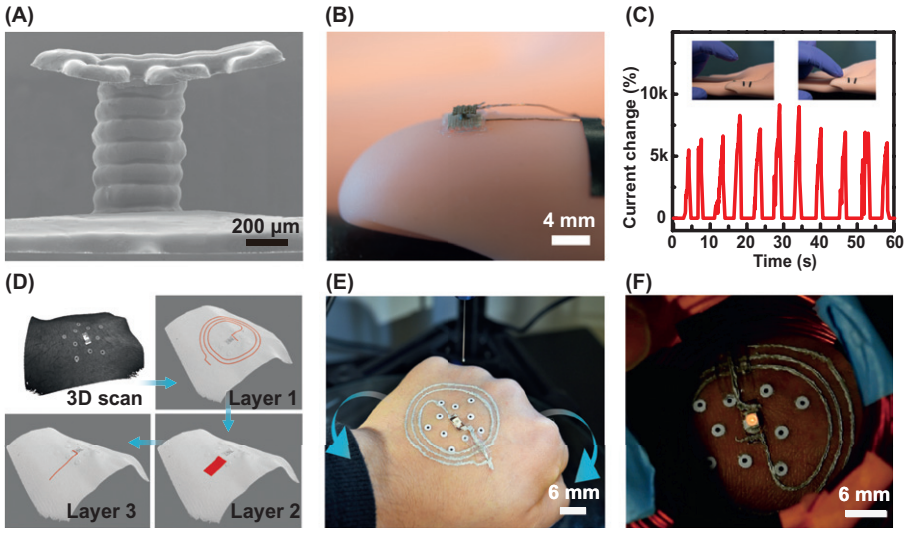

Fig. 13.7 3D printed functional electronic devices on the body. (A–C) 3D printed tactile sensor on the fingertip of a hand model: (A) SEM image of one sensing element; (B) optical image of a fully 3D printed conformal tactile sensor; (C) current response of the tactile sensor upon pressing by a human finger [10]. (D–F) Adaptively 3D printed electronic circuit on the back of a human hand: (D) 3D scanned images showing the topological information of the hand and the toolpaths of each layer of the device; (E) adaptively 3D printed inductive coil on a freely moving hand; (F) the integrated inductive coil connected to a pick-and-place discrete LED, which was wirelessly powered by an external source [14].
Figures (A)–(C) are adapted with permission from S.Z. Guo, K. Qiu, F. Meng, S.H. Park, M.C. McAlpine, 3D printed stretchable tactile sensors, Adv. Mater. 29 (2017) 1701218, © Wiley 2017. Figures (D)–(F) are adapted with permission from Z. Zhu, S.-Z. Guo, T. Hirdler, C. Eide, X. Fan, J. Tolar, M.C. McAlpine, 3D printed functional and biological materials on moving freeform surfaces, *Adv. Mater. 30* (2018) 1707495, © Wiley 2018.

In the case of 3D printed inductive coils, a higher degree of automation has been demonstrated by "adaptively" 3D printing the device onto the back of a human hand undergoing random motions, including translation and rotation. The adaptive 3D printing platform consists of a delta robot and tracking cameras that precisely locate the target surface. The tracking error of the printer can be controlled within 1.5 mm with a feeding speed up to 10 mm/s. As shown in Fig. 13.7D, before printing, one LED was first pick-and-placed by a vacuum-controlled nozzle, and then fiducial markers were attached to the back of the hand as for computer vision–based tracking. Then the hand was 3D scanned via SLS in the format of dense point clouds, so that the conformal toolpath of the inductive coil could be computed and the spatial information of the markers and LED registered in the system. During printing, a Perspective-n-Point (PnP) method was utilized to track the position and orientation of the hand that freely moved within the workspace (ϕ230 mm $\times$ 270 mm (H)) (Fig. 13.7E). Due to the fast curing capability of the active ink as discussed previously, the 3D printed inductive coil was functional 15 min after being printed, proven by lighting up the LED, powered wirelessly with an external transmission coil (Fig. 13.7F). In addition, the 3D printed inductive coil on the human hand could also function as a moisture sensor. Future work will move toward direct printing of active components such as LEDs and other semiconducting-based devices, and moving toward portable technologies for printing active electronics on the body autonomously.

13.4.3 Interface between 3D printed electronics and skin

To directly deposit inks onto human skin for the fabrication of on-body electronics, the toxicity of the materials has to be minimized such that they do not damage or otherwise adversely affect the cells and tissue. Unfortunately, to date, the biocompatibility of most inks that are commonly used for 3D printed electronics is still questionable. For example, although AgNPs are widely used commercially for products such as antimicrobial agents and biosensors [79], various experimental results have revealed the complexity in understanding the toxicity of AgNPs, which results from the wide spectrum of particle size, aggregation, and concentration and consequently, different profiles of bioactivity [80,81]. Both in vivo and in vitro studies have shown that AgNPs in the range of 10–40 nm do not demonstrate cytotoxicity to mice and guinea pigs through oral, ocular, and dermal routes [82–84]. Yet, studies have shown that long-term exposure to AgNPs of 18 nm can cause inflammatory response within the alveoli and alterations in lung functions at all particulate concentrations for laboratory rats [85]. Therefore, the direct use of AgNPs on human tissue needs to be carefully studied and the proper processing of the ink should be performed. Such concerns also exist for other inks based on semiconductor nanoparticles and polymers.

One intermediate way to 3D print electronic devices onto biological tissue is to utilize a thin and conformal substrate onto which the functional devices can be printed. This practice holds two benefits—shielding the surface of the tissue from the inks that may be toxic and creating a smoother surface to print on. The relationship between the thickness of the substrate and conformability to the target surface has been studied by Kim et al. In this model, the device consisting of Au electrode arrays and polyimide (PI) film is simplified to be a thin film with bending stiffness EI, thickness h, width b

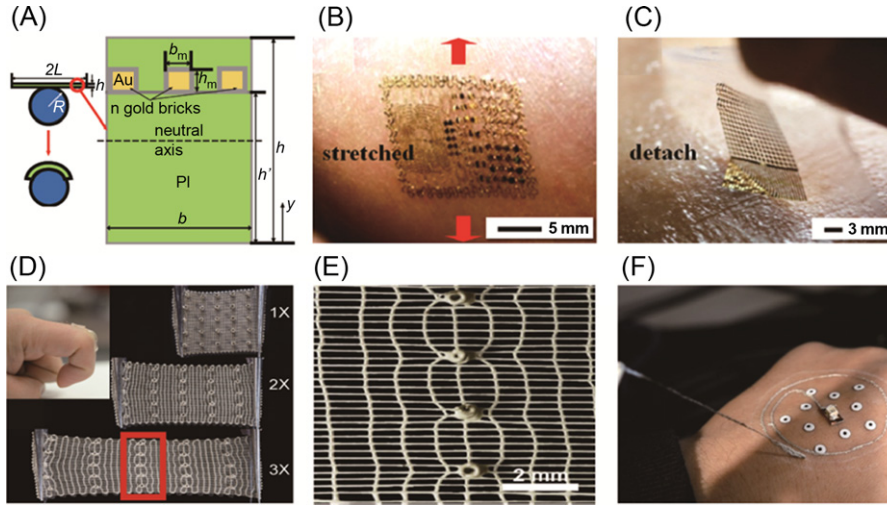

Fig. 13.8 Interfaces between the skin and electronic devices made via microfabrication and 3D printing. (A) Sketches of the unwrapped and wrapped states of thin films onto cylindrical surfaces, and a sketch of the cross-section of the thin film with gold electrodes deposited [86]. (B–C) A multifunctional electronic system mounted onto the skin of the forehead to monitor brain activity: (B) the integrated electronic system remains in intimate contact with the skin when stretched; (C) the electronic system can be easily removed [87]. (D–F) 3D printed electronic devices on the hand for physiological sensing: (D) stretching test of the 3D printed sensing layer (inset: the sensor remains in intimate contact with the skin during bending of the finger); (E) enlarged image of the red box in (D) showing the undistorted structure of the sensing element layer during stretching; (F) a 3D printed inductive coil can be easily peeled off the skin [10,14].
Figure (A) is adapted with permission from D.H. Kim, J. Viventi, J.J. Amsden, J. Xiao, L. Vigeland, Y.S. Kim, J.A. Blanco, B. Panilaitis, E.S. Frechette, D. Contreras, D.L. Kaplan, F.G. Omenetto, Y. Huang, K.C. Hwang, M.R. Zakin, B. Litt, J.A. Rogers, Dissolvable films of silk fibroin for ultrathin conformal bio-integrated electronics, Nat. Mater. 9 (2010) 511–517, © 2012 Macmillan Publishers Limited. Figures (B) and (C) are adapted with permission from S. Wang, M. Li, J. Wu, D.H. Kim, N. Lu, Y. Su, Z. Kang, Y. Huang, J.A. Rogers, Mechanics of epidermal electronics. J. Appl. Mech. 79 (2012) 031022, © 2012 American Society of Mechanical Engineers. Figures (D) and (E) are adapted with permission from S.Z. Guo, K. Qiu, F. Meng, S.H. Park, M.C. McAlpine, 3D printed stretchable tactile sensors, Adv. Mater. 29 (2017) 1701218, © Wiley 2017. Figure (F) is adapted with permission from Z. Zhu, S.-Z. Guo, T. Hirdler, C. Eide, X. Fan, J. Tolar, M.C. McAlpine, 3D printed functional and biological materials on moving freeform surfaces, *Adv. Mater. 30* (2018) 1707495, © Wiley 2018.

and length 2*L*, as illustrated in Fig. 13.8A with a zoom-in view of the cross-section of the device. The bending stiffness *EI* is correlated to the cube of the thickness of the film, h^3 [86],

$$EI \propto f\left(h^3\right) \tag{13.6}$$

For the wrapped state to be energetically favorable,

$$\gamma \geq \gamma_c = \frac{EI}{2R^2 b} \tag{13.7}$$

where γ is the adhesion energy per unit area, which has a value $\sim$10 mJ/m^2 in the set-up [88]. From this relationship, one can determine that for a target surface with a given radius of curvature, the thinner the substrate is, the easier it is for the thin-film device to conform to the surface. Therefore, polymeric thin films with thicknesses on the micrometer scale can be spin-coated and transferred onto target biological surfaces.

For microfabricated epidermal electronics, factors that influence conformal contact between the electronic devices and the target surfaces include the thickness of the substrates and devices, the elastic moduli of the substrate materials, adhesion between the adjacent surfaces, and the surface roughness of the target surfaces [87]. Furthermore, ultrathin conducting/semiconducting elements and serpentine structures patterned on polymeric substrates help increase the flexibility and stretchability of epidermal electronics (Fig. 13.8B). In addition, the interfacial bonding induced by van der Waals adhesion renders facile peel-off of the devices from the target surfaces (Fig. 13.8C).

Direct printing of devices onto target surfaces enables conformal fitting of the devices onto the macroscopic morphology of the surfaces, which may exhibit complex topologies such as curvilinearity. Innovative direct-write functional inks that are highly stretchable and room-temperature curable facilitate intimate contact under stretched and compressed conditions even without specifically designed serpentine patterns, as displayed in Fig. 13.8D and E [10]. Because of the moderate adhesion between PEO and skin, the structures printed with PEO-based active inks can be easily peeled off the skin [14] (Fig. 13.8F). However, at the microscopic scale, the contact between the 3D printed structures and the skin—interfaces determined by factors such as surface roughness, viscosities, and surface tensions of the inks—still needs to be quantitatively studied. Analogous to microfabricated epidermal electronics, interfacial mechanical models that incorporate the properties of inks and biological tissues could help optimize the adhesion, biocompatibility, and performance of 3D printed electronics on the body.

13.5 Conclusion

This chapter introduced recent progress in 3D printed electronic materials from the perspectives of inks, devices, and fundamental mechanics. We also discussed autonomous 3D printing platforms, which will allow a complete "untethering" of electronics from cleanrooms and microfabrication facilities and toward mobile 3D printing even in remote locations. From the perspective of materials, a broad palette of functionalities has already been printed, including conductors, semiconductors, and dielectrics, and properties such as printability, printing conditions, ink compositions, and band diagrams were considered. A continuing expansion of the ink database accompanied by increased tunability of properties will yield more categories of 3D printed electronic devices with improved performances. Fundamentally, capillary

flow that induces inhomogeneity of printed patterns and interfacial mechanics between electronics and human skin was discussed. Further investigations of fluid and interfacial mechanics tailored for direct electronics printing on the body will enable direct-write bioelectronics with augmented performance and comfort.

Acknowledgments

The authors acknowledge the Kortshagen Group in the Mechanical Engineering Department at the University of Minnesota for providing SiNCs for LEDs. The SiNC-LED work was supported primarily by the National Science Foundation through the University of Minnesota MRSEC under Award Number DMR-1420013. Prof. M. C. McAlpine acknowledges the National Institute of Biomedical Imaging and Bioengineering of the National Institutes of Health (Award No. 1DP2EB020537) to support time in writing this chapter. The content is solely the responsibility of the authors and does not necessarily represent the official views of the National Institutes of Health.

References

[1] J. Kim, P. Gutruf, A.M. Chiarelli, S.Y. Heo, K. Cho, Z. Xie, A. Banks, S. Han, K.I. Jang, J.W. Lee, K.T. Lee, X. Feng, Y. Huang, M. Fabiani, G. Gratton, U. Paik, J.A. Rogers, Miniaturized battery-free wireless systems for wearable pulse oximetry, Adv. Funct. Mater. 27 (2017) 1604373.

[2] J.A. Rogers, T. Someya, Y. Huang, Materials and mechanics for stretchable electronics, Science 327 (2010) 1603–1607.

[3] B.H. Kim, M.S. Onses, J.B. Lim, S. Nam, N. Oh, H. Kim, K.J. Yu, J.W. Lee, J.H. Kim, S.K. Kang, C.H. Lee, J. Lee, J.H. Shin, N.H. Kim, C. Leal, M. Shim, J.A. Rogers, High-resolution patterns of quantum dots formed by electrohydrodynamic jet printing for light-emitting diodes, Nano Lett. 15 (2015) 969–973.

[4] M. Singh, H.M. Haverinen, P. Dhagat, G.E. Jabbour, Inkjet printing-process and its applications, Adv. Mater. 22 (2010) 673–685.

[5] P. Calvert, Inkjet printing for materials and devices, Chem. Mater. 13 (2001) 3299–3305.

[6] Y. Zhang, F. Zhang, Z. Yan, Q. Ma, X. Li, Y. Huang, J.A. Rogers, Printing, folding and assembly methods for forming 3D mesostructures in advanced materials, Nat. Rev. Mater. 2 (2017) 17019.

[7] Y.L. Kong, I.A. Tamargo, H. Kim, B.N. Johnson, M.K. Gupta, T.W. Koh, H.A. Chin, D.A. Steingart, B.P. Rand, M.C. McAlpine, 3D printed quantum dot light-emitting diodes, Nano Lett. 14 (2014) 7017–7023.

[8] J.R. Raney, J.A. Lewis, Printing mesoscale architectures, MRS Bull. 40 (2015) 943–950.

[9] M.C. McAlpine, Y.L. Kong, 3D printed active electronic materials and devices. U.S. Patent 9,887,356 issued Feb. 6, 2018, 2018.

[10] S.Z. Guo, K. Qiu, F. Meng, S.H. Park, M.C. McAlpine, 3D printed stretchable tactile sensors, Adv. Mater. 29 (2017) 1701218.

[11] G. Haghiashtiani, E. Habtour, S.-H. Park, F. Gardea, M.C. McAlpine, 3D printed electrically-driven soft actuators, Extreme Mech. Lett. 21 (2018) pp. 1–8.

[12] K. Qiu, Z. Zhao, G. Haghiashtiani, S.-Z. Guo, M. He, R. Su, Z. Zhu, D.B. Bhuiyan, P. Murugan, F. Meng, S.H. Park, C.-C. Chu, B.M. Ogle, D.A. Saltzman, B.R. Konety, R.M. Sweet, M.C. McAlpine, 3D printed organ models with physical properties of tissue and integrated sensors, Adv. Mater. Technol. (2017) 1700235.

[13] M.S. Mannoor, Z. Jiang, T. James, Y.L. Kong, K.A. Malatesta, W.O. Soboyejo, N. Verma, D.H. Gracias, M.C. McAlpine, 3D printed bionic ears, Nano Lett. 13 (2013) 2634–2639.
[14] Z. Zhu, S.-Z. Guo, T. Hirdler, C. Eide, X. Fan, J. Tolar, M.C. McAlpine, 3D printed functional and biological materials on moving freeform surfaces, Adv. Mater. 30 (2018) 1707495.
[15] S. Saunders, MIGO Can 3D Print on the Go With Unique Backpack [Online], Available: https://3dprint.com/196488/makex-kickstarter-success-migo/, 2017 (Accessed 2017).
[16] K. Sun, T.S. Wei, B.Y. Ahn, J.Y. Seo, S.J. Dillon, J.A. Lewis, 3D printing of interdigitated li-ion microbattery architectures, Adv. Mater. 25 (2013) 4539–4543.
[17] N. Zhou, C. Liu, J.A. Lewis, D. Ham, Gigahertz electromagnetic structures via direct ink writing for radio-frequency oscillator and transmitter applications, Adv. Mater. 29 (2017) 1605198.
[18] S.S. Robinson, K.W. O'Brien, H. Zhao, B.N. Peele, C.M. Larson, B.C. Mac Murray, I.M. van Meerbeek, S.N. Dunham, R.F. Shepherd, Integrated soft sensors and elastomeric actuators for tactile machines with kinesthetic sense, Extreme Mech. Lett. 5 (2015) 47–53.
[19] B.Y. Ahn, E.B. Duoss, M.J.G. Motala, Xiaoying, S.-I. Park, Y. Xiong, J.N. Yoon, G. Ralph, J.A. Rogers, J.A. Lewis, Omnidirectional printing of flexible, stretchable, and spanning silver microelectrodes, Science 323 (2009) 1590–1593.
[20] Z. Ying, W. Youhua, L. Runfeng, X. Lin, Z. Qin, H. Yongan, Multichannel noninvasive human-machine interface via stretchable μm thick sEMG patches for robot manipulation, J. Micromech. Microeng. 28 (2018) 014005.
[21] M. Mahto, B. Sniderman, 3D opportunity for electronics Additive manufacturing powers up [Online], Deloitte Insights, 2017. Available from: https://www2.deloitte.com/insights/us/en/focus/3d-opportunity/additive-manufacturing-3d-printed-electronics.html. (Accessed 10 February 2018).
[22] M. Graetzel, R.A.J. Janssen, D.B. Mitzi, E.H. Sargent, Materials interface engineering for solution-processed photovoltaics, Nature 488 (2012) 304–312.
[23] N.J. Jeon, J.H. Noh, Y.C. Kim, W.S. Yang, S. Ryu, S.I. Seok, Solvent engineering for high-performance inorganic-organic hybrid perovskite solar cells, Nat. Mater. 13 (2014) 897–903.
[24] M. Liu, M.B. Johnston, H.J. Snaith, Efficient planar heterojunction perovskite solar cells by vapour deposition, Nature 501 (2013) 395–398.
[25] J.P.J. Markham, S.C. Lo, S.W. Magennis, P.L. Burn, I.D.W. Samuel, High-efficiency green phosphorescence from spin-coated single-layer dendrimer light-emitting diodes, Appl. Phys. Lett. 80 (2002) 2645–2647.
[26] K. Ellmer, Past achievements and future challenges in the development of optically transparent electrodes, Nat. Photonics 6 (2012) 809–817.
[27] J. Lee, H. Jung, J. Lee, D. Lim, K. Yang, J. Yi, W.-C. Song, Growth and characterization of indium tin oxide thin films deposited on PET substrates, Thin Solid Films 516 (2008) 1634–1639.
[28] Z. Chen, W. Li, R. Li, Y. Zhang, G. Xu, H. Cheng, Fabrication of highly transparent and conductive indium-tin oxide thin films with a high figure of merit via solution processing, Langmuir 29 (2013) 13836–13842.
[29] S. Narioka, H. Ishii, D. Yoshimura, M. Sei, Y. Ouchi, K. Seki, S. Hasegawa, T. Miyazaki, Y. Harima, K. Yamashita, The electronic structure and energy level alignment of porphyrin/metal interfaces studied by ultraviolet photoelectron spectroscopy, Appl. Phys. Lett. 67 (1995) 1899–1901.

[30] M.S. White, D.C. Olson, S.E. Shaheen, N. Kopidakis, D.S. Ginley, Inverted bulk-heterojunction organic photovoltaic device using a solution-derived ZnO underlayer, Appl. Phys. Lett. 89 (2006) 143517.
[31] J.H. Burroughes, D.D.C. Bradley, A.R. Brown, R.N. Marks, K. Mackay, R.H. Friend, P.L. Burns, A.B. Holmes, Light-emitting diodes based on conjugated polymers, Nature 347 (1990) 539–541.
[32] R.H. Friend, R.W. Gymer, A.B. Holmes, J.H. Burroughes, R.N. Marks, C. Taliani, D.D.C. Bradley, D.A. Dos Santos, J.L. Brédas, M. Lögdlund, W.R. Salaneck, Electroluminescence in conjugated polymers, Nature 397 (1999) 121–128.
[33] K. He, Y. Liu, J. Gong, P. Zeng, X. Kong, X. Yang, C. Yang, Y. Yu, R. Liang, Q. Ou, Solution processed organic light-emitting diodes using the plasma cross-linking technology, Appl. Surf. Sci. 382 (2016) 288–293.
[34] M.S. White, M. Kaltenbrunner, E.D. Głowacki, K. Gutnichenko, G. Kettlgruber, I. Graz, S. Aazou, C. Ulbricht, D.A.M. Egbe, M.C. Miron, Z. Major, M.C. Scharber, T. Sekitani, T. Someya, S. Bauer, N.S. Sariciftci, Ultrathin, highly flexible and stretchable PLEDs, Nat. Photonics 7 (2013) 811–816.
[35] B.J. Worfolk, S.C. Andrews, S. Park, J. Reinspach, N. Liu, M.F. Toney, S.C. Mannsfeld, Z. Bao, Ultrahigh electrical conductivity in solution-sheared polymeric transparent films, Proc. Natl. Acad. Sci. U. S. A. 112 (2015) 14138–14143.
[36] Y.H. Kim, C. Sachse, M.L. Machala, C. May, L. Müller-Meskamp, K. Leo, Highly conductive PEDOT:PSS electrode with optimized solvent and thermal post-treatment for ITO-free organic solar cells, Adv. Funct. Mater. 21 (2011) 1076–1081.
[37] J. Ouyang, C.W. Chu, F.C. Chen, Q. Xu, Y. Yang, High-conductivity poly(3,4-ethylenedioxythiophene):poly(styrene sulfonate) film and its application in polymer optoelectronic devices, Adv. Funct. Mater. 15 (2005) 203–208.
[38] Y. Xia, K. Sun, J. Ouyang, Solution-processed metallic conducting polymer films as transparent electrode of optoelectronic devices, Adv. Mater. 24 (2012) 2436–2440.
[39] K.Y. Cheng, R. Anthony, U.R. Kortshagen, R.J. Holmes, High-efficiency silicon nanocrystal light-emitting devices, Nano Lett. 11 (2011) 1952–1956.
[40] L. Qian, Y. Zheng, J. Xue, P.H. Holloway, Stable and efficient quantum-dot light-emitting diodes based on solution-processed multilayer structures, Nat. Photonics 5 (2011) 543–548.
[41] C. Ladd, J.H. So, J. Muth, M.D. Dickey, 3D printing of free standing liquid metal microstructures, Adv. Mater. 25 (2013) 5081–5085.
[42] J.W. Boley, E.L. White, G.T.C. Chiu, R.K. Kramer, Direct writing of gallium-indium alloy for stretchable electronics, Adv. Funct. Mater. 24 (2014) 3501–3507.
[43] M.D. Dickey, R.C. Chiechi, R.J. Larsen, E.A. Weiss, D.A. Weitz, G.M. Whitesides, Eutectic gallium-indium (EGaIn): a liquid metal alloy for the formation of stable structures in microchannels at room temperature, Adv. Funct. Mater. 18 (2008) 1097–1104.
[44] P. Hapala, K. Kůsová, I. Pelant, P. Jelínek, Theoretical analysis of electronic band structure of 2- to 3-nm Si nanocrystals, Phys. Rev. B 87 (2013) 195420.
[45] T.-H. Kim, S. Jun, K.-S. Cho, B.L. Choi, E. Jang, Bright and stable quantum dots and their applications in full-color displays, MRS Bull. 38 (2013) 712–720.
[46] S.J. Lim, M.U. Zahid, P. Le, L. Ma, D. Entenberg, A.S. Harney, J. Condeelis, A.M. Smith, Brightness-equalized quantum dots, Nat. Commun. 6 (2015) 8210.
[47] O. Chen, J. Zhao, V.P. Chauhan, J. Cui, C. Wong, D.K. Harris, H. Wei, H.S. Han, D. Fukumura, R.K. Jain, M.G. Bawendi, Compact high-quality CdSe-CdS core-shell nanocrystals with narrow emission linewidths and suppressed blinking, Nat. Mater. 12 (2013) 445–451.

[48] Wikipedia-Contributors, Quantum dot [Online], Wikipedia, The Free Encyclopedia, 2018. Available from: https://en.wikipedia.org/wiki/Quantum_dot. (Accessed 30 January 2018).
[49] B.G. Lee, J.W. Luo, N.R. Neale, M.C. Beard, D. Hiller, M. Zacharias, P. Stradins, A. Zunger, Quasi-direct optical transitions in silicon nanocrystals with intensity exceeding the bulk, Nano Lett. 16 (2016) 1583–1589.
[50] H.M. Haverinen, R.A. Myllylä, G.E. Jabbour, Inkjet printed RGB quantum dot-hybrid LED, J. Disp. Technol. 6 (2010) 87–89.
[51] R.D. Deegan, O. Bakajin, T.F. Dupont, G. Huber, S.R. Nagel, T.A. Witten, Capillary flow as the cause of ring stains from dried liquid drops, Nature 389 (1997) 827–829.
[52] J. Park, J. Moon, Control of colloidal particle deposit patterns within picoliter droplets ejected by ink-jet printing, Langmuir 22 (2006) 3506–3513.
[53] K.H. Kang, H.C. Lim, H.W. Lee, S.J. Lee, Evaporation-induced saline Rayleigh convection inside a colloidal droplet, Phys. Fluids 25 (2013) 042001.
[54] J.C. Maxell, Science Papers, Cambridge University Press, Cambridge, 1890.
[55] J.D. Jackson, Classical Electrodynamics, Wiley, New York, 1975.
[56] L. Zhan, S.Z. Guo, F. Song, Y. Gong, F. Xu, D.R. Boulware, M.C. McAlpine, W.C.W. Chan, J.C. Bischof, The role of nanoparticle design in determining analytical performance of lateral flow immunoassays, Nano Lett. (2017).
[57] U.R. Kortshagen, R.M. Sankaran, R.N. Pereira, S.L. Girshick, J.J. Wu, E.S. Aydil, Nonthermal plasma synthesis of nanocrystals: fundamental principles, materials, and applications, Chem. Rev. 116 (2016) 11061–11127.
[58] T. Zhu, K. Shanmugasundaram, S.C. Price, J. Ruzyllo, F. Zhang, J. Xu, S.E. Mohney, Q. Zhang, A.Y. Wang, Mist fabrication of light emitting diodes with colloidal nanocrystal quantum dots, Appl. Phys. Lett. 92 (2008) 023111.
[59] J.H. Ahn, H.S. Kim, K.J. Lee, S. Jeon, S.J. Kang, Y. Sun, R.G. Nuzzo, J.A. Rogers, Heterogeneous three-dimensional electronics by use of printed semiconductor nanomaterials, Science 314 (2006) 1754–1757.
[60] U. Resch-Genger, M. Grabolle, S. Cavaliere-Jaricot, R. Nitschke, T. Nann, Quantum dots versus organic dyes as fluorescent labels, Nat. Methods 5 (2008) 763–775.
[61] F. Erogbogbo, K.-T. Yong, I. Roy, R. Hu, W.-C. Law, W. Zhao, H. Ding, F. Wu, R. Kumar, M.T. Swihart, P.N. Prasad, In vivo targeted cancer imaging, sentinel lymph node mapping and multi-channel imaging with biocompatible silicon nanocrystals, ACS Nano 5 (2011) 413–423.
[62] Z.F. Li, E. Ruckenstein, Water-soluble poly(acrylic acid) grafted luminescent silicon nanoparticles and their use as fluorescent biological staining labels, Nano Lett. 4 (2004) 1463–1467.
[63] Y.-S. Chen, B.-T. Chen, Measuring of a three-dimensional surface by use of a spatial distance computation, Appl. Opt. 42 (2003) 1958–1972.
[64] D.-H. Kim, N. Lu, R. Ma, Y.-S. Kim, R.-H. Kim, S. Wang, J. Wu, S.M. Won, H. Tao, A. Islam, K.J. Yu, T.-I. Kim, R. Chowdhury, M. Ying, L. Xu, M. Li, H.-J. Chung, H. Keum, M. Mccormick, P. Liu, Y.-W. Zhang, F.G. Omenetto, Y. Huang, T. Coleman, J.A. Rogers, Epidermal electronics, Science 333 (2011) 838–843.
[65] M.S. Lee, K. Lee, S.Y. Kim, H. Lee, J. Park, K.H. Choi, H.K. Kim, D.G. Kim, D.Y. Lee, S. Nam, J.U. Park, High-performance, transparent, and stretchable electrodes using graphene-metal nanowire hybrid structures, Nano Lett. 13 (2013) 2814–2821.
[66] H. Yao, A.J. Shum, M. Cowan, I. Lahdesmaki, B.A. Parviz, A contact lens with embedded sensor for monitoring tear glucose level, Biosens. Bioelectron. 26 (2011) 3290–3296.

[67] J.T. Muth, D.M. Vogt, R.L. Truby, Y. Menguc, D.B. Kolesky, R.J. Wood, J.A. Lewis, Embedded 3D printing of strain sensors within highly stretchable elastomers, Adv. Mater. 26 (2014) 6307–6312.
[68] M. Stoppa, A. Chiolerio, Wearable electronics and smart textiles: a critical review, Sensors 14 (2014) 11957–11992.
[69] P.D. Mitcheson, E.M. Yeatman, G.K. Rao, A.S. Holmes, T.C. Green, Energy harvesting from human and machine motion for wireless electronic devices, Proc. IEEE 96 (2008) 1457–1486.
[70] C. Hou, H. Wang, Q. Zhang, Y. Li, M. Zhu, Highly conductive, flexible, and compressible all-graphene passive electronic skin for sensing human touch, Adv. Mater. 26 (2014) 5018–5024.
[71] A. Frutiger, J.T. Muth, D.M. Vogt, Y. Menguc, A. Campo, A.D. Valentine, C.J. Walsh, J.A. Lewis, Capacitive soft strain sensors via multicore-shell fiber printing, Adv. Mater. 27 (2015) 2440–2446.
[72] A. Kidane, G.C. Lantz, S. Jo, K. Park, Surface modification with PEO-containing triblock copolymer for improved biocompatibility: in vitro and ex vivo studies, J. Biomater. Sci. Polym. Ed. 10 (1999) 1089–1105.
[73] F. Kreppel, S. Kochanek, Modification of adenovirus gene transfer vectors with synthetic polymers: a scientific review and technical guide, Mol. Ther. 16 (2008) 16–29.
[74] C. Edwards, R. Marks, Evaluation of biomechanical properties of human skin, Clin. Dermatol. 13 (1995) 375–380.
[75] D. Roy, N. Wettels, G.E. Loeb, Elastomeric skin selection for a fluid-filled artificial fingertip, J. Appl. Polym. Sci. 127 (2013) 4624–4633.
[76] C.S. Boland, U. Khan, G. Ryan, S. Barwich, R. Charifou, A. Harvey, C. Backes, Z. Li, M.S. Ferreira, M.E. Möbius, R.J. Young, J.N. Coleman, Sensitive electromechanical sensors using viscoelastic graphene-polymer nanocomposites, Science 354 (2016) 1257–1260.
[77] X. Li, R. Zhang, W. Yu, K. Wang, J. Wei, D. Wu, A. Cao, Z. Li, Y. Cheng, Q. Zheng, R.S. Ruoff, H. Zhu, Stretchable and highly sensitive graphene-on-polymer strain sensors, Sci. Rep. 2 (2012) 870.
[78] J.L. Tanner, D. Mousadakos, P. Broutas, S. Chatzandroulis, Y.S. Raptis, D. Tsoukalas, Nanoparticle strain sensor, Procedia Eng. 25 (2011) 635–638.
[79] A. Katsumiti, D. Gilliland, I. Arostegui, M.P. Cajaraville, Mechanisms of toxicity of Ag nanoparticles in comparison to bulk and ionic Ag on mussel hemocytes and gill cells, PLoS ONE 10 (2015) e0129039.
[80] P.V. Asharani, W. Yi Lian, G. Zhiyuan, V. Suresh, Toxicity of silver nanoparticles in zebrafish models, Nanotechnology 19 (2008)255102.
[81] L.G. Ovington, The truth about silver, Ostomy Wound Mange. 50 (2004) 1–10.
[82] Y. Liu, Z. Zheng, J.N. Zara, C. Hsu, D.E. Soofer, K.S. Lee, R.K. Siu, L.S. Miller, X. Zhang, D. Carpenter, C. Wang, K. Ting, C. Soo, The antimicrobial and osteoinductive properties of silver nanoparticle/poly(DL-lactic-co-glycolic acid)-coated stainless steel, Biomaterials 33 (2012) 8745–8756.
[83] P. Maneewattanapinyo, W. Banlunara, C. Thammacharoen, S. Ekgasit, T. Kaewamatawong, An evaluation of acute toxicity of colloidal silver nanoparticles, J. Vet. Med. Sci. 73 (2011) 1417–1423.
[84] Z. Zheng, W. Yin, J.N. Zara, W. Li, J. Kwak, R. Mamidi, M. Lee, R.K. Siu, R. Ngo, J. Wang, D. Carpenter, X. Zhang, B. Wu, K. Ting, C. Soo, The use of BMP-2 coupled—nanosilver-PLGA composite grafts to induce bone repair in grossly infected segmental defects, Biomaterials 31 (2010) 9293–9300.

[85] J.H. Sung, J.H. Ji, J.D. Park, J.U. Yoon, D.S. Kim, K.S. Jeon, M.Y. Song, J. Jeong, B. S. Han, J.H. Han, Y.H. Chung, H.K. Chang, J.H. Lee, M.H. Cho, B.J. Kelman, I.J. Yu, Subchronic inhalation toxicity of silver nanoparticles, Toxicol. Sci. 108 (2009) 452–461.

[86] D.H. Kim, J. Viventi, J.J. Amsden, J. Xiao, L. Vigeland, Y.S. Kim, J.A. Blanco, B. Panilaitis, E.S. Frechette, D. Contreras, D.L. Kaplan, F.G. Omenetto, Y. Huang, K. C. Hwang, M.R. Zakin, B. Litt, J.A. Rogers, Dissolvable films of silk fibroin for ultrathin conformal bio-integrated electronics, Nat. Mater. 9 (2010) 511–517.

[87] S. Wang, M. Li, J. Wu, D.H. Kim, N. Lu, Y. Su, Z. Kang, Y. Huang, J.A. Rogers, Mechanics of epidermal electronics, J. Appl. Mech. 79 (2012).

[88] M. Chaudhury, G. Whitesides, Direct measurement of interfacial interactions between semispherical lenses and flat sheets of poly(dimethylsiloxane) and their chemical derivatives, Langmuir 7 (1991) 1013–1023.